Journal of Power Sources 195 (2010) 7295–7301

Contents lists available at ScienceDirect

Journal of Power Sources

journal homepage: www.elsevier.com/locate/jpowsour

Stability of Ni–yttria stabilized zirconia anodes based on Ni-impregnation

Trine Klemensø*, Karl Thydén, Ming Chen, Hsiang-Jen Wang

Fuel Cells and Solid State Chemistry Division, Risø National Laboratory for Sustainable Energy, Technical University of Denmark - DTU, Frederiksborgvej 339, P.O. Box 49, DK-4000 Roskilde, Denmark

ARTICLE INFO

Article history:
Received 26 March 2010
Received in revised form 21 May 2010
Accepted 25 May 2010
Available online 31 May 2010

Keywords:
Fuel cells
SOFC
Ni–YSZ
Impregnation
Sintering

ABSTRACT

Sintering of Ni is a key stability issue for Ni–YSZ anodes, and especially infiltration based electrodes. The potential of MgO, Al_2O_3, TiO_2, CeO_2 and $Ce_{0.90}Gd_{0.10}O_{1.95}$ (CGO10) as sintering inhibitors was investigated for infiltrated Ni based anode structures. The structures were prepared from tape cast porous YSZ layers that were impregnated with Ni to form an electronic percolating phase. The Ni–YSZ structure was subsequently impregnated with the inhibitor candidate, and the stability of the structure was evaluated from conductivity measurements. Lower conductivity degradation rates were observed for samples infiltrated with the inhibitor candidates, and the best inhibitor effect was seen with higher loadings of CGO10, and CeO_2 showed similar potential. The degradation in conductivity was not visibly reflected in the microstructure as Ni coarsening in any of the cases. An adverse effect of MgO, TiO_2 and Al_2O_3 was reduced conductivity, possibly due to reaction with Ni and the formation of higher resistive phases. The Ni-infiltrated anodes were shown to have better initial electrochemical performance at 650 °C than conventionally produced Ni–YSZ anodes, but still very poor stability, and further improvement of the inhibitor approach is necessary before applying the Ni-infiltrated anodes in SOFCs.

1. Introduction

Implementing infiltration steps into the processing route of solid oxide fuel cell (SOFC) has been proven to be very promising. Improved electrochemical performance of impregnated anodes [1–6], and cathodes [1–4,7–10] has been reported, as well as improved redox tolerance [11,12], and since the infiltration steps occur post-sintering, it opens up the choice of materials for all cell components [13,14].

Conventionally, Ni–YSZ (yttria stabilized zirconia) anodes are produced by wet processing techniques where powders of NiO and YSZ are mixed. Infiltration based Ni–YSZ anodes are prepared by impregnating the nickel into a porous YSZ backbone [11,15]. An advantage of the infiltrated Ni–YSZ anode is the lower Ni content required to obtain electronic percolation. For this structure, percolation is obtained already around 9 vol% Ni, whereas 30 vol% Ni is required for percolation with the conventional powder based method with 1 μm sized Ni powder [16–19]. The lower Ni content of the impregnation based anode can explain the improved redox tolerance of the cells as shown in [11].

Sintering of the percolating Ni phase is the main degradation mechanism for Ni–YSZ anodes, and the sintering is more pronounced for the infiltration based anodes, where the Ni particles are much finer and in the nano-size range [12,20]. Increased stability of a Ni-infiltrated anode was reported in [20], where the infiltration steps were combined with temperature treatments (i.e. Ni precoarsening) at temperatures above the operational temperature. However, the increased stability was on the expense of additional process steps and poorer electrode performance with both higher ohmic and polarisation resistance.

Impeded Ni sintering of conventional 1 μm Ni–YSZ anodes has been reported, when the structure was impregnated with doped ceria or zirconia [21]. The impregnated phase was observed to coat the Ni particle surfaces, and was stated to inhibit the agglomeration. However, the stabilizing effect of the impregnations was only evaluated from microscopy on samples that had not experienced any longer term testing. In addition to the possible sintering inhibitor properties, impregnated doped ceria further has the advantage of improving the electrode performance [1,2,4,5], as well as the sulphur tolerance of the electrode [1,2].

Ni sintering inhibition by impregnation of a second ceramic phase may also be a possibility for Ni impregnated Ni–YSZ anodes. Especially, for impregnated electrodes targeted for operation at intermediate temperatures, where the driving force for sintering of the nano-sized particles is weaker [22]. The purpose of this work was to investigate the potential of impregnated MgO, Al_2O_3, TiO_2, CeO_2 and $Ce_{0.90}Gd_{0.10}O_{1.95}$ (CGO10) as Ni sintering inhibitors for Ni impregnated Ni–YSZ anodes working at intermediate SOFC temperatures. In addition, the effect of the porous YSZ was considered by using two different backbone structures, and the effect of the inhibitor loading was also considered. The sintering was mainly studied by direct current conductivity measurements, which is

* Corresponding author. Tel.: +45 4677 5756; fax: +45 4677 5858.
E-mail address: trkl@risoe.dtu.dk (T. Klemensø).

0378-7753/$ – see front matter © 2010 Elsevier B.V. All rights reserved.
doi:10.1016/j.jpowsour.2010.05.047

known to be a useful tool for characterizing the connected Ni phase and the sintering process of Ni–YSZ cermets [23–25].

2. Experimental

Porous layers of YSZ were produced by tape casting 8 mol% Y_2O_3 stabilized ZrO_2 powder (TZ-8Y, Tosoh Co., Tokyo, Japan) and 50 vol% graphite (Graphit Kropfmühl AG, Hauzenberg, Germany), which is the most common pore former for fabricating porous backbones, see e.g. [12,26]. In some cases, 10 wt% of 8YSZ precursor gel was added, which also acts as pore former. The precursor gel was made from $ZrO(NO_3)_2{\cdot}6H_2O$ and $Y(NO_3)_3{\cdot}6H_2O$ (in molar ratio to form 8YSZ), and $C_2H_6O_2$, HNO_3 and water (ratio 133:42:30) as solvents, and was gelled at 80 °C before added to the slurry. The samples based on only graphite are denoted "G", and the samples with graphite plus precursor gel are denoted "GP".

The powders were processed into ethanol based slurries, using PEI 10000 (polyethylenimine) as dispersant, and a PVB-based (polyvinyl butyral) binder system as described in [27], and the slurries were tape cast. The dried green tapes were punched and cut into strip shaped samples, and subsequently sintered at 1220 °C into sizes of ca. 35 mm × 5 mm × 0.3 mm.

The sintered strips were impregnated with molten $Ni(NO_3)_2{\cdot}6H_2O$ at 80 °C under the influence of vacuum. The infiltrations were repeated to obtain a nickel loading of ca. 10 vol%, and upon each infiltration the nitrate was decomposed to oxide at 300 °C. At least 10 cycles of infiltration and nitrate-oxide conversions were necessary.

Following the nickel impregnations, vacuum assisted infiltrations with precursor solutions of the sintering inhibitor candidates were carried out. Aqueous 3 M solutions of the precursor salts $Ce(NO_3)_3{\cdot}6H_2O$, $Gd(NO_3)_3{\cdot}6H_2O$, $Al(NO_3)_3{\cdot}9H_2O$, $Mg(NO_3)_2{\cdot}6H_2O$, and $C_{12}H_{20}O_{12}Ti$ were prepared, and added a minor amount of a surfactant, essentially following the general procedure set forth previously in, e.g. [12,26]. Between 1 and 3 infiltrations with precursor solutions were done, and upon each infiltration the precursor was decomposed at 350 °C, except for the titania precursor that was decomposed at 450 °C.

A four-electrode setup was applied for the DC conductivity measurements. The sample was placed on top of a ceramic support plate for mechanical handling, and current electrodes were mounted at the sample ends, by wrapping platinum wire around the joined sample and support plate. To ensure contact, the wires were guided by grooves cut into the support plate, and Pt paste was painted around the electrodes. The potential probes are fixed in the setup (spaced 10 mm apart), and is contacted to the sample by a load. The sample was placed so the potential probes touch around the sample centre. Upon mounting, the sample was briefly heated in air to 700 °C to sinter the Pt paste, after which the temperature was reduced to 650 °C. At 650 °C the setup was flushed with N_2 before reducing the sample in 97% H_2–3% H_2O with a flow of 150 ml min^{-1}. Following the reduction, the resistance was measured for ca. 200 h with 5–15 min intervals. The data was acquired using a Keithley 2700 multimeter (Keithley Instruments Inc., Cleveland, OH).

The microstructure of the sintered, impregnated and tested samples was examined by electron microscopy using a Hitachi TM-1000 (Pleasanton, CA), and a high-resolution FESEM (Supra 35 from Carl Zeiss, Germany). One of the tested samples was further examined by transmission electron microscopy (TEM). The TEM instrument used was a JEM-3000F equipped with a field-emission gun and an EDS microanalysis detector with an ultra-thin window as well as the software system Oxford Instruments INCA. A 100 nm thick TEM lamella was prepared by use of the "lift-out" technique in a Crossbeam 1540XB dual focused ion beam (FIB)/SEM from Carl Zeiss, Germany [28].

The porosity of the backbone structures was measured with an Autopore IV 9500 V1.05 instrument from Micromeritics Instrument Corporation (Norcross, GA), and thermo gravimetric analysis of the precursor decomposition process was performed on a Seiko TG/DTA 320 U (Seiko Instruments Inc., Tokyo, Japan). The infiltrated phases were attempted identified using an X-ray diffractometer (STOE Theta–Theta diffractometer), and the X-ray diffractograms were collected at $15^\circ \leq 2\theta \leq 80^\circ$ using Cu Kα radiation.

Symmetric cells of the infiltrated anodes were produced by laminating the green porous YSZ layers on both sides of a thick electrolyte (ca. 140 μm), and the infiltrations with Ni and inhibitor precursors were performed post-sintering according to the routine described previously. The cells were prepared and tested as described in [29], using electrochemical impedance spectroscopy at 650 °C in an atmosphere of 97% H_2 + 3% H_2O (100 ml min^{-1}).

3. Results

3.1. Characterization of the porous structures

The open porosity of the produced structures was characterized by mercury porosimetry, and the profiles of the two structures are shown in Fig. 1. Much finer porosity was seen for structure G compared to GP, with the median pore diameter being 0.27 and 0.90 μm. Furthermore, lower open porosity was seen for G (27%) compared to GP (43%). The coarser and higher porosity of GP was confirmed by microscopy on the polished cross-sections of the sintered structures, shown in Fig. 2.

3.2. Thermogravimetry

The 10 cycles of impregnation and decomposition of Ni nitrate are the most time-consuming steps in the sample fabrication route, and the preparation time can be minimized if the minimum decomposition temperature is identified. A thermogravimetric analysis of the Ni nitrate was carried out, and the profile is shown in Fig. 3. It was seen that the water and nitrate groups were removed at 300 °C, and that heat treatment to this temperature should be sufficient to form the NiO.

3.3. Characterization of the impregnation

The theoretical amount of Ni in vol%, deposited after the *i*th impregnation–decomposition and reduction (Ni $[v/o]_i$) can be cal-

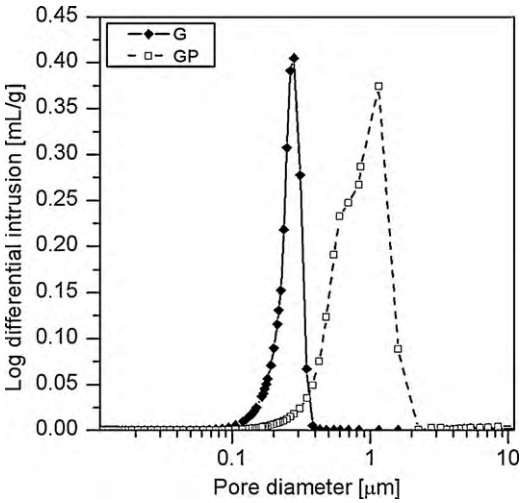

Fig. 1. Mercury porosimetry profiles of the sintered porous structures.

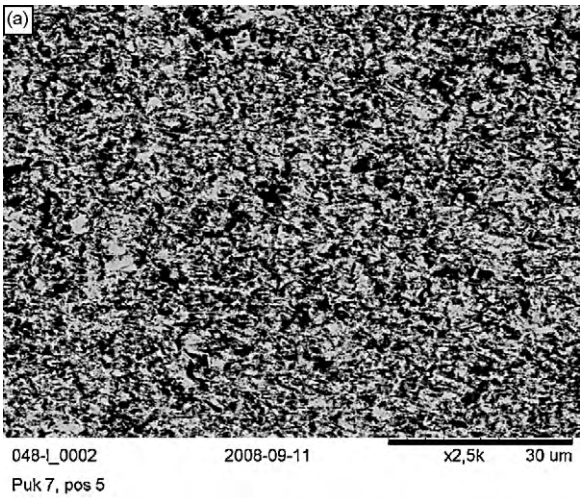

Fig. 2. Micrographs of the sintered porous structures G (a) and GP (b).

culated as shown in Eq. (1) below:

$$\mathrm{Ni[v/o]}_i = \frac{\rho_{\mathrm{sol}} \cdot c_{\mathrm{Ni}}}{\rho_{\mathrm{Ni}}} \cdot \left(\varepsilon_0 + \sum_{i=2}^{i} \left(\varepsilon_{i-1} - \varepsilon_{i-1} \cdot \frac{\rho_{\mathrm{sol}} \cdot c_{\mathrm{Ni}} \cdot M_{\mathrm{NiO}}}{\rho_{\mathrm{NiO}} \cdot M_{\mathrm{Ni}}} \right) \right) \times 100\% \qquad (1)$$

The equation assumes all open pores to be filled with the solution upon each infiltration, and it also assumes complete conversion of the precursor to NiO upon decomposition. M denotes the molecular mass ($M_{\mathrm{NiO}} = 74.71\ \mathrm{g\,mol^{-1}}$, $M_{\mathrm{Ni}} = 58.69\ \mathrm{g\,mol^{-1}}$,), ρ is the density

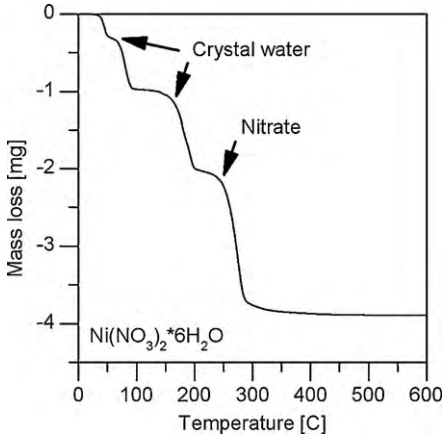

Fig. 3. Thermogravimetric profile of $Ni(NO_3)_2{\cdot}6H_2O$.

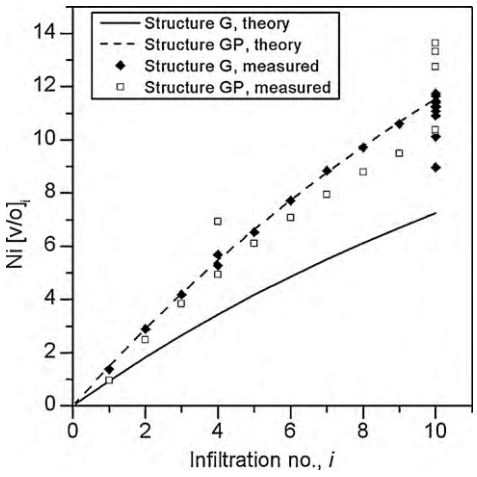

Fig. 4. Calculated and measured Ni content in vol% as a function of the number of impregnations.

($\rho_{\mathrm{NiO}} = 6.67\ \mathrm{g\,cm^{-3}}$, $\rho_{\mathrm{Ni}} = 8.907\ \mathrm{g\,cm^{-3}}$), ε_0 is the start porosity, ε_i is the porosity after the ith impregnation, and ρ_{sol} and c_{Ni} are the density and Ni content in wt% of the Ni-solution, respectively. The theoretical Ni content based on Eq. (1) as a function of number of infiltrations for the two fabricated porous structures is shown in Fig. 4, where the solid curve represents G, and the dashed GP. The higher Ni content of GP is explained by the higher start porosity, and for structure G, the calculated Ni content is seen to be below the percolation threshold of 9 vol% even after 10 impregnations.

The Ni content of the infiltrated samples was also measured. The content was derived from the measured weight gains after the impregnations, and the measured sample dimensions. The measurements are included in Fig. 4, with closed diamonds for G, and open squares for GP. For structure G, the measurements were generally higher than the corresponding point on the theoretical curve and above the 9 vol% after 10 impregnation cycles. For GP on the other hand, the measurements were generally slightly below the theoretical curve. Furthermore, a significant scatter was seen between samples subjected to 10 infiltrations. Measurement points above the theoretical curve indicated that the pores were completely filled upon impregnation, and a maximum in Ni gain was achieved. The Ni surplus compared to the theoretical value could be due to measurement uncertainties, both in dimensions and porosity, and deposited material on the sample surface. However, points below the theoretical curves, as well as the scattering after the 10th impregnation, indicated that the pores in some cases were not completely filled, or that the liquid solution to some extent had flowed out of the sample during the drying/decomposition step. The latter was supported by the fact that only GP samples, with the coarser and more porous structure, showed measurements below the theoretical curve.

The amount of infiltrated sintering inhibitor was also evaluated based on the weight gain. The weight gains, and corresponding wt% and vol% of the oxide, are summarized in Table 1.

Since the cation concentration of all the precursor solutions was similar, the same amount of cation moles was impregnated. However, due to the different molar weight and density of the cations and oxides, this resulted in different wt% and vol% of the inhibitor oxides. Samples with both high and low CGO10 load were prepared by impregnating various times.

3.4. XRD (X-ray diffractometer)

The infiltrated samples were analyzed with XRD to check for reactions or solid solutions between the infiltrated inhibitors and

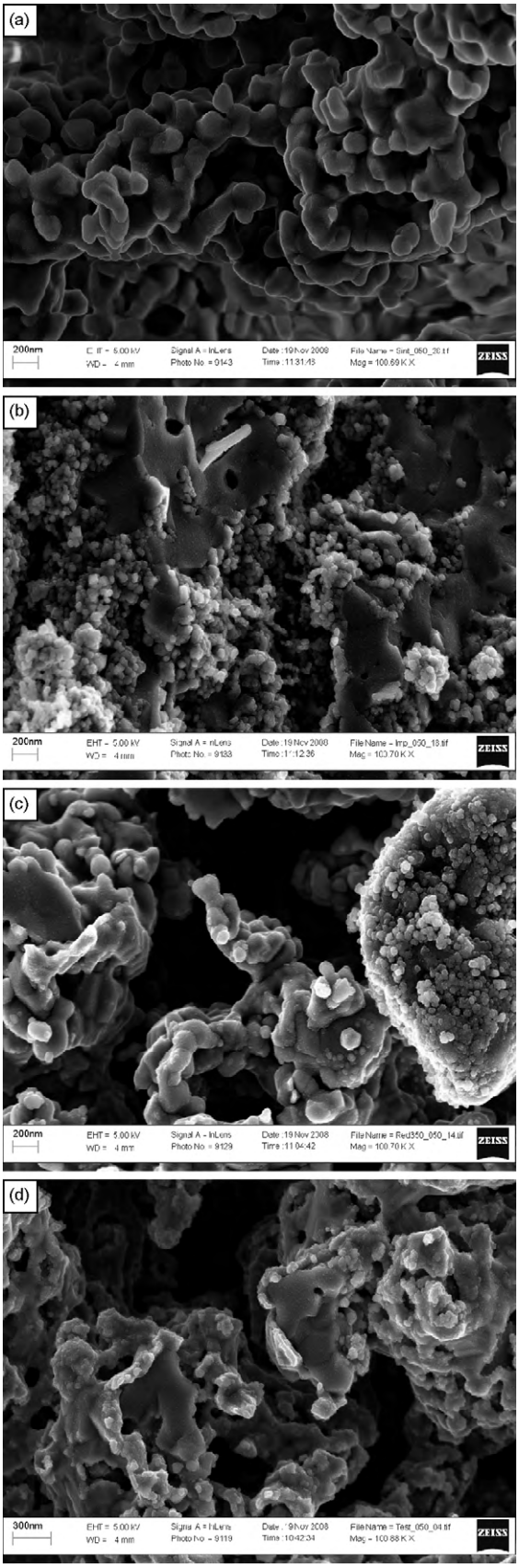

Fig. 5. Micrographs of the GP structure with 13.33 vol% Ni. (a) Sintered, (b) infiltrated with NiO, (c) reduced, (d) after test including a redox cycle.

the Ni. No reaction products were identified from the diffractograms (not shown here), indicating that they are either absent, or if present, their amounts are below the XRD detection limit (which is about 1 wt%).

3.5. SEM (scanning electron microscopy)

The microstructures of the sintered, infiltrated, reduced and tested samples were examined with SEM. As an example, the microstructures of GP with 13.33% Ni are illustrated in Fig. 5. The size of the individual Ni particles situated on the surface of the YSZ backbone appeared to be in the same range, around 52 nm, both before and after test (cf. Fig. 5c and d). No visible Ni coarsening was observed for any of the microstructures.

3.6. TEM (transmission electron microscopy)

It was not possible to discern the inhibitors from the infiltrated Ni phase in SEM-EDS. However, with TEM-EDS this was possible. The tested sample with a high loading of CGO10 inhibitor was prepared for TEM, and an area of 7 μm × 12 μm was investigated. It was generally seen that the CGO10 nano particles were located on top of the Ni film as illustrated in Fig. 6, where Zr is shown in red, Ni in yellow, and Ce in blue. Furthermore, the high-resolution TEM imaging showed that the Ni particles were polycrystalline with average crystalline domains around 10 nm. Similarly for CGO, but with a bit bigger crystalline domains around 20 nm.

3.7. DC (direct current) conductivity measurements

The measured conductivity of samples containing only impregnated nickel is shown in Fig. 7 (for structure G), and Fig. 8 (for

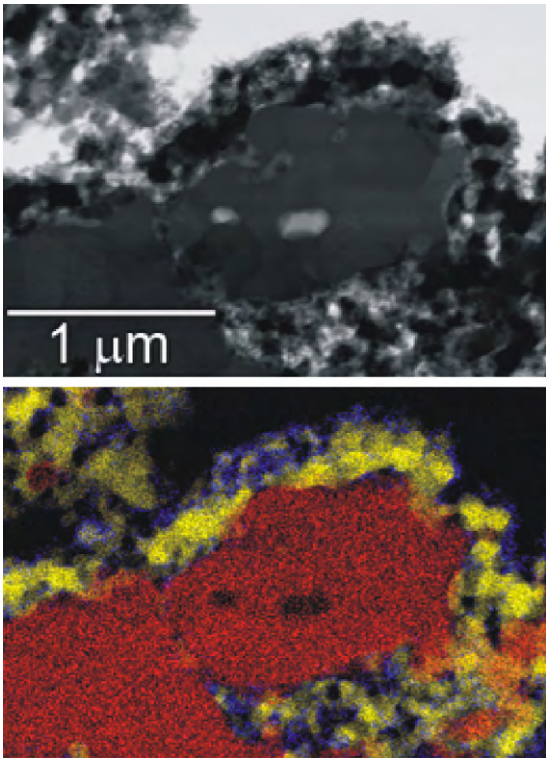

Fig. 6. TEM on the tested sample with CGO10 high loading. A bright-field image of the EDS analyzed area is shown at the top, and below the combined EDS results with the three phases represented as red (Zr), yellow (Ni) and blue (Ce). (For interpretation of the references to color in this figure legend, the reader is referred to the web version of the article.)

Table 1
Infiltrated amounts of sintering inhibitors.

Inhibitor	M_{cation} (g mol^{-1})	δ_{oxide} (g cm^{-3})	Structure G			Structure GP		
			m (mg)	Wt%	Vol%	*m* (mg)	w/o	v/o
CGO10	141.83	7.3	4.81	2.64	1.61	6.31	3.75	2.04
CGO10	141.83	7.3	9.92	5.01	3.13	19.89	10.31	5.86
CeO_2	140.12	7.3	8.64	4.36	2.65	–	–	–
TiO_2	47.88	4.23	0.8	0.46	0.47	6.33	3.89	3.60
Al_2O_3	26.98	3.965	2.28	1.22	1.29	–	–	–
MgO	24.31	3.58	2.60	1.45	1.75	–	–	–

GP). For both structures, the Ni content was seen to be decisive for the start conductivity and the degradation. In both cases, higher Ni content was observed to result in higher start conductivity. For G, the initial degradation (within the first 24 h of test) was worse the lower the Ni content, but the long-term degradation was less severe with the lower Ni loads. For GP, the same general degradation trend was seen between the high Ni loaded samples (long dashed curve), and the low Ni loaded sample (fine dashed curve), however for a intermediate Ni loaded sample (solid curve) and a lower loaded sample (gray curve), lower initial and long-term degradation were observed. The variation and scatter in the start conductivities indicated proximity to the percolation threshold, which was further indicated when comparing the start conductivities as a function of the Ni content as shown in Fig. 9.

Due to the proximity to the percolation limit, it was important to consider the Ni content when evaluating the effect of the inhibitors. The measured conductivity profiles of the samples impregnated with inhibitor candidates are shown in Figs. 10 and 11, and for comparison, the reference samples with similar Ni contents were included (shown as black or gray curves). For both structures, and in all cases, the inhibitor appeared to diminish the degradation. For G, higher loadings of CGO10 (red curve, Fig. 10) or CeO_2 (purple curve) seemed to be efficient inhibitors while maintaining the

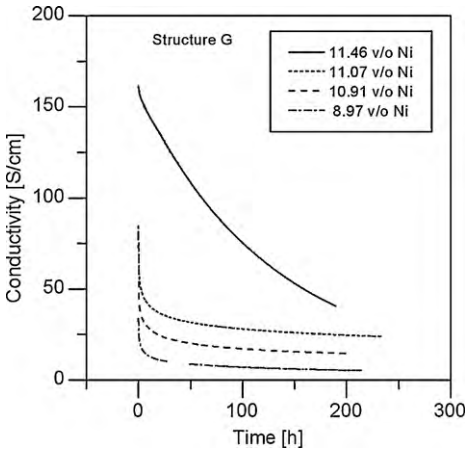

Fig. 7. Conductivity profiles over time for Ni-infiltrated structures of the type G. The amount of infiltrated Ni in vol% is indicated in the legend.

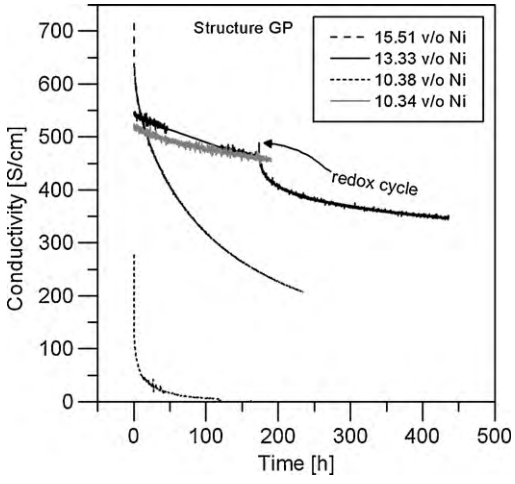

Fig. 8. Conductivity profiles for Ni-infiltrated structures of the type GP. The amount of infiltrated Ni in vol% is indicated in the legend. A redox cycle was carried out after the first 190 h of test of the sample with 13.33% Ni (indicated with arrow).

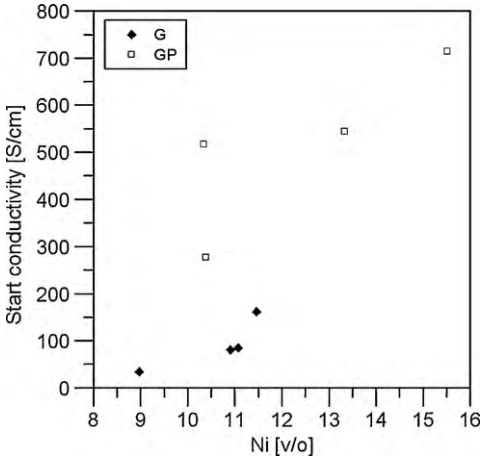

Fig. 9. Start conductivity as a function of Ni content.

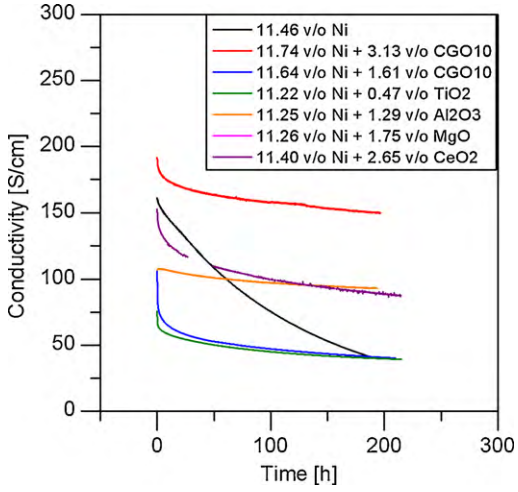

Fig. 10. Conductivity profiles of structure G impregnated with the various inhibitor candidates. A reference sample with similar Ni content is included for comparison (black curve). (For interpretation of the references to color in this figure legend, the reader is referred to the web version of the article.)

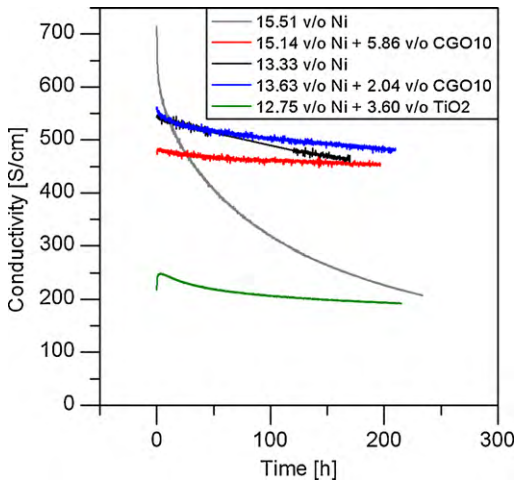

Fig. 11. Conductivity profiles of GP structures impregnated with inhibitors. Reference samples with similar Ni contents are included for comparison (black and gray curve). (For interpretation of the references to color in this figure legend, the reader is referred to the web version of the article.)

start conductivity level. The apparent slightly lower effect of CeO_2 compared to CGO high loading, is possibly an effect of the lower CeO_2 content (cf. Fig. 10), but could also reflect changes in the ceria surface properties associated with the Gd doping. For GP, the same trend occurred, with higher loadings of CGO10 (red curve, Fig. 11) having the highest impact.

The diminished degradation when using especially alumina (yellow curve), but also titania (green curve), was counterbalanced by lower start conductivities (cf. Figs. 10 and 11), and particularly for the case with magnesia, the conductivity decreased to almost zero (pink curve not visible in Fig. 10). The adverse effect of alumina, titania and especially magnesia might be due to reactions with Ni and the formation of higher resistive phases, e.g. poorly conducting spinels. It is however difficult to verify formation of these phases using XRD or SEM and EDS, due to the very low concentrations of the inhibitors (TiO_2, Al_2O_3, MgO) used in the present work.

3.8. Electrochemical impedance spectroscopy

The electrochemical performance of the infiltrated symmetric cells was in most cases difficult to determine due to rapid degradation even at 650 °C. However, the initial performance of the Ni-infiltrated anodes was very promising. The initial performance of a Ni impregnated sample with a low content CGO as sintering inhibitor is shown in Fig. 12, and for comparison the spectrum of a conventional Ni–YSZ anode [29] at the same temperature is shown. The infiltrated anode appeared well performing (around 0.25 Ω cm^2), and better than the conventional anode. Contrary to

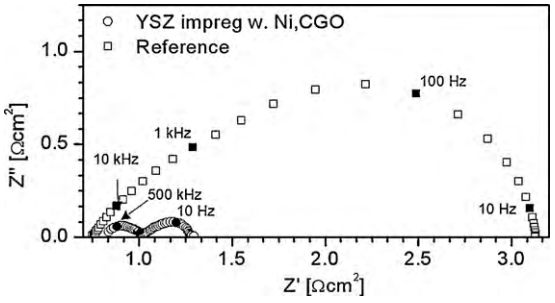

Fig. 12. Impedance spectrum at 650 °C in 97% H_2–3% H_2O of a symmetric cell fabricated with Ni and low load CGO impregnation. For comparison the spectra of a conventional Ni–YSZ anode from Ref. [29] is shown.

the referenced sample, part of the polarisation appeared related to very high frequency process/processes (summit frequency around 500 kHz). However, the degradation was quite severe. After only 24 h at 650 °C, it had degraded about a factor of 10 (not shown here).

4. Discussion and conclusions

The main processing issue with the Ni impregnated anodes is the time-consuming impregnation–decomposition steps. At least 10 cycles are necessary, even when as in this work, the process is optimized by using the solution with the maximum Ni concentration (hot infiltration with molten Ni nitrate, instead of an aqueous nitrate solution that can be infiltrated at room temperature), and minimum heat treatment for decomposing the nitrate.

Furthermore, after 10 cycles, the Ni content still appeared to be close to the percolation threshold. This resulted in large differences in the conductivity level for even minor differences in the Ni content, and will likely complicate up-scaling and reproducibility of the method.

The Ni impregnated structures showed degradation that depended on the Ni content, whereas the two different backbone structures seemed to have minor effect on the degradation. For both structures, the initial degradation (as observed within the first 24 h of test) was generally worse the lower the Ni content, but the long-term degradation less severe. This observation may be explained by the degree of contacts between Ni particles. At low Ni loadings the sintering is more critical for the percolation, but as the sintering proceeds and most contacts are lost, the sintering will slow down, as the Ni sintering primarily takes place by Ni surface diffusion at elevated temperatures [23]. The lowest degradation was observed for intermediate-low Ni loaded samples, where the best trade-off appeared to exist between a sufficient percolation degree (i.e. the initial sintering was less critical), and long-term contact degree.

Based on the conductivity measurements, Al_2O_3, TiO_2, CeO_2 and CGO10 all showed potential as Ni sintering inhibitors, and a higher impact was indicated for higher inhibitor loadings. The effect of the inhibitors was indicated to be due to their microstructural position on top of the Ni film thereby impeding Ni sintering by surface diffusion, i.e. a mechanism similar to the one set forth in [21]. Unfortunately, TiO_2 and Al_2O_3, and particularly MgO, was indicated to react with Ni and/or other elements, forming higher resistive phases and decreasing the overall conductivity. Though no clear evidence of the presence of resistive phases was found, and the amounts must be below the XRD detection limit, even small amounts can be detrimental for the conductivity, especially for structures like these, where the electronic conduction path is a thin film, and the structure is close to the percolation threshold. In conclusion, the most appropriate inhibitors among the tested candidates are CGO10 and CeO_2, with CGO10 having additional potential advantages with respect to the catalytic reaction and sulphur tolerance as mentioned in the introduction.

The degradation in conductivity was not visibly reflected as coarsening in the microstructure. As seen with SEM, the Ni particle size was around 52 nm both before and after test, even for a structure without sintering inhibitor (cf. Fig. 5), indicating that coalescence is not the main sintering mechanism. In combination with the polycrystallinity of the Ni, this makes it difficult to get any microstructural evidence of the sintering occurring. XRD and TEM imaging will only estimate the change in Ni crystallite size, thus to achieve a full estimate of the microstructural changes, high-resolution SEM in combination with longer experimental times than done in this work, will be required.

Contrary to the microstructural observations, the degradation in conductivity was clearly reflected in the electrochemical perfor-

mance. Though the Ni-infiltrated anodes performed initially better at 650 °C than conventionally produced Ni–YSZ anodes, the stability was very poor even at a time scale below 24 h. The EIS measurements do not consider the Ni sintering process isolated, but the higher sensitivity of the technique towards the Ni sintering makes it an important technique for future evaluation of Ni impregnated anodes. In conclusion, the Ni sintering inhibitor approach must be further improved before it can be applied with advantage in Ni–YSZ anodes.

Acknowledgements

We acknowledge Marianne Nielsen for assistance with ceramic processing and tape casting, Mohan Menon for suggestions in ceramic processing and the precursor gel fabrication, and Carsten Gynther Sørensen for technical support to the thermal analysis. The financial support from Energinet.dk under ForskEL project 2008-1-0045 is greatly acknowledged.

References

[1] T.Z. Sholklapper, H. Kurokawa, C.P. Jacobsen, S.J. Visco, L.C. De Jonghe, Nano Lett. 7 (7) (2007) 2136.
[2] T.Z. Sholklapper, H. Kurokawa, C.P. Jacobsen, S.J. Visco, L.C. De Jonghe, ECS Trans. 7 (1) (2007) 837.
[3] S.P. Jiang, Mater. Sci. Eng. A 418 (1/2) (2006) 199.
[4] S.P. Jiang, S. Zhang, Y.D. Zhen, W. Wang, J. Am. Ceram. Soc. 88 (7) (2005) 1779.
[5] J. Qiao, K. Sun, N. Zhang, B. Sun, J. Kong, D. Zhou, J. Power Sources 169 (2007) 253.
[6] X. Lou, Z. Liu, S. Wang, Y. Xiu, C.P. Wong, M. Liu, J. Power Sources 195 (2010) 419.
[7] J.M. Vohs, R.J. Gorte, Adv. Mater. 21 (2009) 943.
[8] K. Yamahara, C.P. Jacobsen, S.J. Visco, X.-F. Zhang, L.C. De Jonghe, Solid State Ionics 176 (2005) 275.
[9] Y. Huang, J.M. Vohs, R.J. Gorte, J. Electrochem. Soc. 152 (7) (2005) A1347.
[10] Y. Huang, J.M. Vohs, R.J. Gorte, J. Electrochem. Soc. 151 (4) (2004) A646.
[11] A.N. Busawon, D. Sarantaridis, A. Atkinson, Electrochem. Solid-State Lett. 11 (10) (2008) B186.
[12] M.C. Tucker, G.Y. Lau, C.P. Jacobsen, L.C. De Jonghe, S.J. Visco, J. Power Sources 171 (2) (2007) 477.
[13] M.C. Tucker, G.Y. Lau, C.P. Jacobsen, L.C. De Jonghe, S.J. Visco, ECS Trans. 7 (1) (2007) 279.
[14] M.C. Tucker, J. Power Sources 195 (15) (2010) 4570.
[15] R.M.C. Clemmer, S.F. Corbin, Solid State Ionics 166 (2004) 251.
[16] S.F. Corbin, X. Qiao, J. Am. Ceram. Soc. 86 (3) (2003) 403.
[17] R.M.C. Clemmer, S.F. Corbin, Solid State Ionics 180 (2009) 721.
[18] F.H. Wang, R.S. Guo, Q.T. Wei, Y. Zhou, H.L. Li, S.L. Li, Mater. Lett 58 (2004) 3079.
[19] M.C. Tucker, G.Y. Lau, C.P. Jacobsen, L.C. De Jonghe, S.J. Visco, J. Power Sources 175 (2008) 447.
[20] C.A. Singh, V.V. Krishan, ECS Trans. 6 (21) (2008) 25.
[21] S.P. Jiang, Y.Y. Duan, J.G. Love, J. Electrochem. Soc. 149 (9) (2002) A1175.
[22] T.Z. Sholklapper, V. Radmilovic, C.P. Jacobsen, S.J. Visco, L.C. De Jonghe, Electrochem. Solid-State Lett. 10 (4) (2007) B74.
[23] T. Klemensø, M. Mogensen, J. Am. Ceram. Soc. 90 (11) (2007) 3582.
[24] D. Simwonis, F. Tietz, D. Stöver, Solid State Ionics 132 (2000) 241.
[25] R.J. Aaberg, R. Tunold, F.W. Poulsen, N. Bonanos, in: B. Thorstensen (Ed.), Proceedings of the 2nd European SOFC Forum, PV 1, 1996, p. 363.
[26] T.Z. Sholklapper, C. Lu, C.P. Jacobsen, S.J. Visco, L.C. De Jonghe, Electrochemical and Solid-State Lett. 9 (8) (2006) A376.
[27] T. Klemensø, M. Menon, S. Ramousse, Ceram. Int. 36 (2010) 773.
[28] A. Grosjean, O. Sanséau, V. Radmilovic, A. Thorel, Solid State Ionics 177 (2006) 1977–1980.
[29] M. Pihlatie, T. Ramos, A. Kaiser, J. Power Sources 193 (2009) 322.